

Contents lists available at ScienceDirect

# **Engineering Fracture Mechanics**

journal homepage: www.elsevier.com/locate/engfracmech



# Mechanical response of 3D printed irregular sutural tessellations with Voronoi tile patterns under tension



Shujing Dong, Richard J. Nash, Yaning Li<sup>\*</sup>

Department of Mechanical and Industrial Engineering, Northeastern University, Boston, MA, United States

## ARTICLE INFO

Keywords: Voronoi pattern Suture Fracture Finite element analysis 3D Printing

## ABSTRACT

The mechanical response of bio-inspired irregular sutural tessellations with Voronoi tile patterns are designed and fabricated via multi-material 3D printing. The effective mechanical properties of the designs were characterized via uni-axial tension mechanical experiments on the 3D printed specimens. Systematic nonlinear finite element simulations are conducted to explore the damage initiation and evolution of the designs. The influences of important design parameters, including tile length aspect ratio R, tile size irregularity  $C_{std}$ , suture amplitude irregularity  $A_{std}$ , and stiffness ratio between the soft and hard phases, were evaluated. The effective stiffness, Poisson's ratio, strength, toughness, and failure mechanisms are systematically quantified. The results demonstrate that an optimized level of suture irregularity exists for maximizing the modulus of toughness. The results provide a general design guideline for designing functionally graded two-phase tessellations with high mechanical performance.

## 1. Introduction

The Voronoi pattern, named after the mathematician Georgy Voronoy [1], represents a fascinating geometric concept that has found diverse applications in material design. Originating in the early 20th century, Voronoi patterns emerged from Voronoy's work on partitioning a space into regions based on the proximity to a set of seed points [2,3]. These regions, known as Voronoi cells or polygons, possess intricate boundaries determined by the nearest seed point. In material design, Voronoi patterns have become instrumental in understanding microstructural characteristics and optimizing material properties [4]. By analyzing Voronoi tessellations in various materials such as metals [5], ceramics [6], and polymers [7], researchers gain insights into grain boundaries, porosity, and mechanical behavior [4,8,9]. For example, In the realm of metallurgy, Voronoi patterns emerge as a result of grain boundary formation during solidification processes in metallic materials [10]. As molten metal cools and solidifies, grains of crystalline structure develop, each with its own distinct orientation and growth rate. Voronoi tessellation naturally arises as these grains compete for space, leading to the formation of irregularly shaped regions delineated by grain boundaries [11]. The study of Voronoi patterns in metallurgy provides valuable insights into material properties such as strength, ductility, and corrosion resistance, as well as influencing factors like cooling rates and alloy compositions [12,13].

Voronoi patterns are also ubiquitous in nature, inspiring novel approaches in biomimetic design, where natural structures like bone tissue and plant cell walls serve as models for the development of lightweight, strong, and adaptive materials [14]. Tessellated composites in nature present a captivating intersection of biological form and function, showcasing intricate patterns and structures

E-mail address: y.li@northeastern.edu (Y. Li).

Corresponding author.

Γ

 $f_h$ 

Ε

n

 $\sigma_{D}$ 

Toughness

Peak stress

Young's modulus

Volume fraction of the hard phase

Power law hardening index

#### Nomenclature Hard phase h Soft phase i $C_{std}$ Standard deviation of the diameter of Voronoi cells R Length aspect ratio of Voronoi cells Wavelength λ Α **Amplitude** In-plane thickness of soft suture layer t Stress along X direction $\sigma_{xx}$ Stress along Y direction $\sigma_{yy}$ Strain along X direction $\hat{I}\mu_{xx}$ $\hat{I}\mu_{yy}$ Strain along Y direction Strain $\sigma$ Stress $A_c$ Amplitude near the vicinity of the vertex Standard deviation of the amplitude of sutures $A_{std}$ Young's modulus of the hard phase $E_h$ $E_i$ Young's modulus of the soft phase $\overline{E}$ Overall stiffness Poisson's ratio of the soft phase $\nu_i$

that have evolved over millions of years to optimize performance and efficiency. These composites, often found in biological materials such as shells [15], bones [16], and plant cell walls [17], exhibit a remarkable array of Voronoi tessellation patterns, where individual elements interlock seamlessly to form a unified structure. Inspired by the principles of tessellation, nature's designs maximize strength, flexibility, and lightweight construction while minimizing material usage. From the hexagonal arrangement of bee honeycombs [18] to the radial symmetry of diatom shells [19], tessellated composites exemplify the ingenuity of natural engineering, offering inspiration and insights for biomimetic design in various fields, including architecture, materials science, and engineering. Studying these natural marvels not only deepens our understanding of biological systems but also fuels innovation in the development of sustainable, efficient, and resilient materials for human applications.

Different from micro-structured engineering materials with flat-edged Voronoi patterns, many Voronoi tessellations in natural composites possess wavy tile boundaries, named as suture interfaces, such as the seedcoats of Potulaca [20] and Common Millets [21], turtle carapace [22], and box fish armors [23]. Wavy suture joints are characterized by their undulating interface where two adjoining materials interlock in a zigzag pattern [24–29]. This arrangement not only distributes stress more evenly but also enhances energy absorption and fracture resistance, making it an ideal template for engineering robust materials. Inspired by nature's design, researchers and engineers are exploring applications of wavy suture joints in material design, particularly for developing lightweight yet durable composites, impact-resistant structures, and flexible biomimetic materials [30–34]. By mimicking the principles of wavy suture joints, novel manufacturing techniques such as 3D printing and composite fabrication are being developed to create advanced materials with superior mechanical properties and multifunctional capabilities [35]. For example, mechanical performance of 3D printed periodic hexagonal wavy sutural tessellation were shown to have simultaneously amplified strength and toughness, and also show negative Poisson's ratio in a certain design space. The effects of irregular morphology on the mechanical behavior of biological sutures were explored and it is revealed that the prevalence of irregular suture morphology in nature is a merit.

In this paper, irregular sutural tessellations with Voronoi tile patterns are designed and fabricated via multi-material 3D printing. Compared with other tessellated composites, wavy suture interface is a unique feature of suture tessellations. However, it is not known that how suture irregularity and the geometry of Voronoi tiles jointly influence the overall mechanical properties of suture tessellations. According to the rules of mixtures, in general, it is expected that the stiffness ratio of hard and soft phases, and tile length aspect ratio are key parameters to determine the overall mechanical properties of tessellated composites. In the current study, for suture tessellations, we introduced more design parameters such as suture irregularity and suture amplitude beyond the general ones. Incorporating Voronoi diagram and wavy sutural tessellation, the effects of tile length aspect ratio, tile size irregularity, suture amplitude irregularity, and stiffness ratio between the soft and hard phases, were evaluated. The effective mechanical properties and fracture behaviors of the designs were characterized via uni-axial tension mechanical experiments on the 3D printed specimens and systematic nonlinear FE simulations. The specimen designs are illustrated in Section 2.1. Section 2.2 and 2.3 focuses on the experimental and FE simulations methods. The major results are presented in Section 3.

# 2. Materials and methods

# 2.1. The geometry of material designs

Inspired by sutural tessellations in nature [20–22], the general two-dimensional structure of the material designed includes two phases, the relatively stiff tiles with polygonal shape and thin, soft layers connecting them. The hard phase and the soft phase are represented by h and i, respectively. The resulting 2D tessellations can be delineated based on overall morphological characteristics of stiff tiles and soft suture layers, such as tile patterns, sizes, size distribution, the length aspect ratio of tiles [36], and the waviness of the soft layer. Based on tile patterns designed, the material tessellations can be categorized into regular and irregular ones (Fig. 1). The irregular tessellations are represented by Voronoi diagram and/or irregular wavy suture layers with spatially varying layer amplitude, as shown in Fig. 1.

The Voronoi diagram is characterized by the standard deviation of the diameter of cells marked by  $C_{std}$  and the length aspect ratio R of hard tiles. As shown in Fig. 1., when  $C_{std} = 0$ , the pattern becomes a regular hexagonal one, and when  $C_{std}$  increases, the Voronoi pattern becomes more irregular. The mean diameter of tiles is kept the same (10 mm) in all designs. In general, the soft wavy suture layers are with a constant wavelength  $\lambda = 1.6$  mm and spatially varying amplitude A. The in-plane thickness t of the suture layer is also kept the same for all designs (t = 0.3 mm). In a Voronoi diagram, vertices typically feature three converging edges, with instances of four edges meeting at a vertex being less common. In order to avoid the penetration of suture layers at the Voronoi vertex and enhance the stability and integrity of the Voronoi structure, we have incorporated a modification involving the reduction of the waviness amplitude, denoted as  $A_{t,t}$  in the vicinity of the vertex.

To systematically analyze the mechanical behaviors of this type of sutural tessellations, four distinct design types are proposed, as shown in Fig. 1. As shown in Fig. 1, generally, Types I, II, and III represent designs with irregular Voronoi pattern but regular suture layers, and Type IV represents designs with both irregular Voronoi pattern and irregular suture layers.

Specifically, Type I incorporates an irregular Voronoi pattern with  $C_{std} = 0.002$  mm, and tile length aspect ratio R = 1. While the regular suture layers are with a constant amplitude A set at 0, 1.0, and 1.5 mm respectively. Type II represents designs with an irregular Voronoi pattern with  $C_{std} = 0.002$  mm, and constant suture amplitude A = 1.0 mm, but varying tile length aspect ratio R = 1, 2, and 3, respectively. Type III focuses on varying  $C_{std}$  of the Voronoi patterns,  $C_{std} = 0.002$ , 0.02, 0.2 and 2 mm, respectively. While the tile length aspect ratio R and the suture amplitude A are kept the same, R = 1 and A = 1.0 mm. Type IV represents designs with an irregular Voronoi pattern with  $C_{std} = 2$  mm, and constant tile length aspect ratio R = 1, but irregular suture layer with amplitude A varying around the average value of 1.0 mm with standard deviation of  $A_{std} = 0.1$ , 0.25, and 0.5 mm, respectively. In addition, the design with regular hexagonal pattern (i.e.  $C_{std} = 0$ , and the R = 1.15) and regular suture layers with constant amplitude A = 1 mm always can serve as a reference design to the irregular ones in Types 1-IV.

For all designs, the mean diameter of the tiles is 10 mm. The in-plane thickness t of the soft interfacial layer is 0.3 mm. Specific design parameters for each type of design are summarized in Table 1.

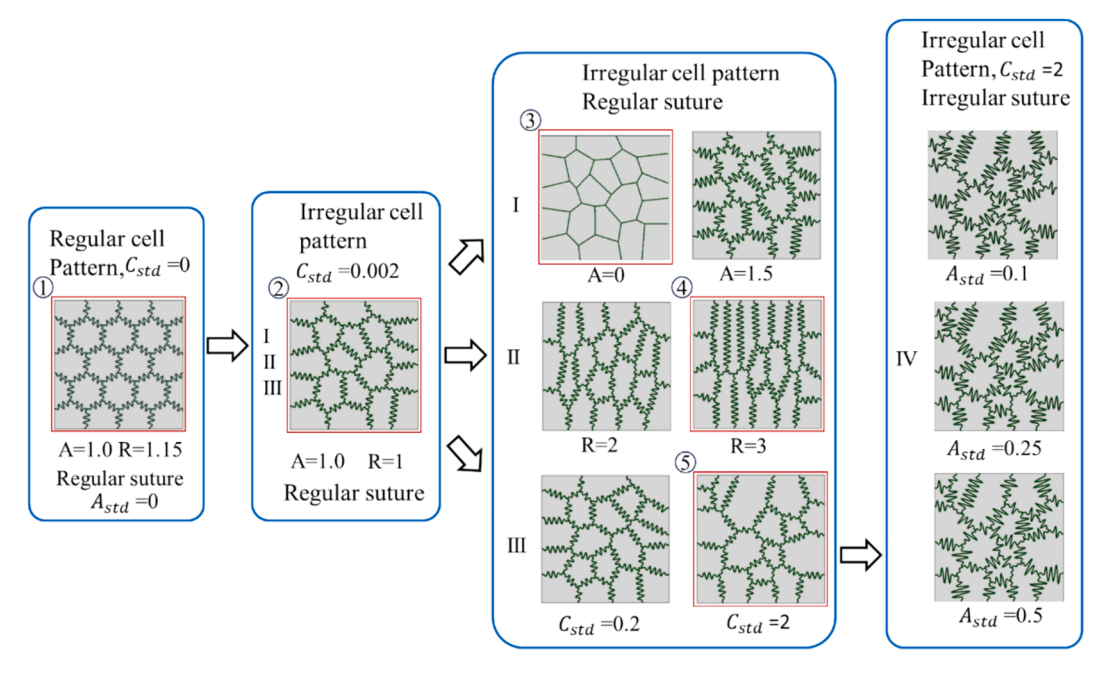


Fig. 1. The geometric designs of the sutural tessellations. The hard and soft phase is represented by light grey and dark green, respectively.

# 2.2. Mechanical experiments on 3D printed specimens

Five designs were selected and fabricated using a multi-material 3D printer (Stratasys Objet260 Connex3). The five designs are highlighted in red frames on Fig. 1: 1. Regular hexagonal tile pattern and regular suture; 2. Irregular Voronoi pattern with  $C_{std} = 0.002$  mm, and regular suture; 3. The design with A = 0 in Type I; 4. The design with R = 3 in Type II. 5. The design with  $C_{std} = 2$  mm in Type III

On each specimen, the area with designed patterns is with dimensions measuring 40 mm x 40 mm x 2 mm, where 2 mm is the out-of-plane thickness of the plate-like specimen. To facilitate gripping during uni-axial tension, for each specimen, a 40 mm-long shoulder part was printed as the hard phase on each side of the design area as shown in Fig. 2a. The hard phase is printed as the model material VeroWhitePlus, and the soft suture layer is printed as another model material TangoBlackPlus. The 3D printer (Stratasys Connex3) can print up to three base resins in a single build. We used the two basic resins (VeroWhitePlus and TangoBlackPlus) in the specimens. The spatial resolution of the 3D printer is about 85  $\mu$ m in XY axes and 30  $\mu$ m in the Z axis. This results in overall model accuracy up to 0.1 mm. We chose the soft layer thickness to be 0.3 mm to achieve precise printing.

To characterize the effective mechanical properties of the designs in two orthogonal directions, each design was tested in two orthogonal loading directions. Uniaxial tension experiments along each loading direction were performed for all five designs. For each experiment, the overall stress strain curve and the effective Poisson's ratio versus overall strain were measured. Black and white speckle patterning was applied to the testing area of each sample (Fig. 2b) and images were taken at even intervals throughout the experiments to track the overall strain and strain contour of each sample using digital image correlation (DIC). We applied the speckle pattern after preparing the surface of specimens. This involved cleaning it with water and drying it with tissues to ensure proper adhesion. A high-contrast speckle pattern was then created using black and white paint to achieve a random distribution of speckles. The average speckle size is approximately  $125 \,\mu\text{m}$ , which is much smaller than the dimensions of the soft phase. The soft suture layer has an in-plane thickness of  $0.3 \, \text{mm}$ . This ensures that the speckles are small enough to capture deformations within the soft phase.

In the uni-axial tension, depicted in Fig. 3a, displacement-control loading conditions are employed at a strain rate of 0.001/s. The gripping arrangement, detailed in Fig. 3b, involves centering and securing the specimen between the upper and lower grips. A single camera equipped with 100 mm F2.8 FF MACRO lens (KENKO TOKINA USA INC) is positioned 901.7 mm from the sample and manually leveled and aligned perpendicular to specimen surface. Two LED light sources (NL 660 model) are positioned on either side of the specimen for a uniform illumination during experiments. The digital magnification factor for the single camera system is 0.33 (107 pixels/mm). The events of specimen deformation were recorded by using SpinView 2.5.0.80 software. Images are captured at 53 ms intervals, with an exposure time of 6.155 ms and no gain.

The VIC-2D software (version 7, Correlated Solutions, USA) is employed to compare images and to obtain displacement and strain. As the distance between the camera and the sample is sufficiently large, the strain errors from out of plane motion are negligible. All the parameters related to the DIC analysis [37] are summarized in Table 2.

# 2.3. Finite element simulations

Finite element (FE) models of all designs were developed in ABAQUS/CAE. The original 2D Voronoi diagrams were created in open-source code Neper [38], and an in-house python code was developed to create the suture geometries based on the Voronoi diagrams. FE simulations of all models were performed in ABAQUS/Implicit with a quasi-static application. In order to determine the effective mechanical properties of the soft suture layer, an integrated experimental and FE simulation method was employed [39]. The Young's modulus of the hard phase and soft phase are determined as 1850 MPa and 50 MPa, respectively. A J2-flow plasticity model with power law hardening (with characterized index of 0.71) was used to model the hard phase. A bilinear hardening model was employed to model the soft interfacial layer. A ductile damage model included in ABAQUS was used to model the damage initiation and evolution in both hard and soft materials. Define the evolution of displacement damage by establishing damage as a function of plastic displacement subsequent to damage initiation. The details for the simulations are summarized in Appendix A.

For all designs, the model consists of 20 Voronoi cells. Fig. 1 shows the original FE models with different design parameters. All models underwent tension deformation along X and Y direction respectively, with the bottom edge being fixed and ramp displacements being applied at the top edge of the FE models. Utilizing a progressively increasing displacement proves more advantageous than applying force, as it simplifies the convergence of the solution algorithm beyond the limit load. The quasi-static analysis was adopted to better observe the failure mechanism.

**Table 1**Geometric parameters of Type I-IV designs.

Designs	$C_{std}$ (mm)	(I II III) A (mm) (IV) $A_{std}$ (mm)	R	t (mm)	λ(mm)	$A_c(mm)$
I	0.002	0, 1.0, 1.5	1	0.3	1.6	0.3
II	0.002	1.0	1, 2, 3			
III	0 (R = 1.15), 0.002, 0.02, 0.2, 2	1.0	1			
IV	0, 2	0.1, 0.25, 0.5	1			

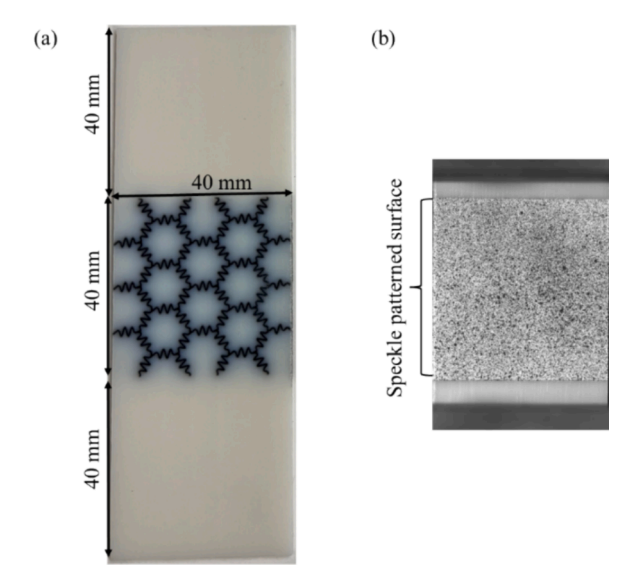


Fig. 2. (a) The 3D printed specimen. (b) The 3D printed specimen with the speckle pattern for DIC.

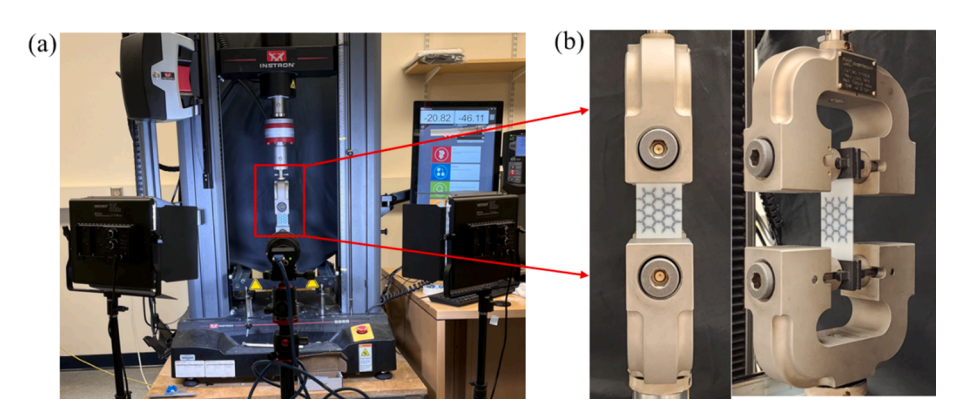


Fig. 3. (a) Uni-axial tensile experimental set-up. (b) Gripping arrangements of sample.

**Table 2** Parameters used in the VIC-2D software.

Average speckle size (pixels)	Digital magnification (pixels/mm)	Subset size (pixel x pixel)	Subset spacing (pixel)
6 (125 μm)	35.4	47x47	5

# 3. Results

To explore the mechanical responses of tiled composites, a combination of experimental testing and FE simulations is utilized. Liu et al. studied the effects of irregularity on the mechanical behavior of single interdigitated biological sutures [40]. Given that material yielding is a consequence of distortion primarily influenced by shear stresses [41], von Mises stress contour and strain distribution are used to evaluate the deformation response and fracture initiation. An approach in defining a yield point is to apply an offset strain, and the tensile yield strength is often defined as 0.2 % offset yield strength [42]. For evaluation of the modulus of toughness, researchers have used the area under stress strain curves as a measure of modulus of toughness of materials [43,44].

# 3.1. The effects of suture amplitudes (Type I designs)

First, to verify the FE approach in simulating damage and failure explained in Section 2.3, both uni-axial tension and FE simulations were conducted on 3D printed specimens of type I designs in two orthogonal directions. The experimental and FE results are shown in Fig. 4a and 4c. Fig. 4a and 4c show that when loaded in X and Y directions, cracks are mainly following the flat suture layer. The FE results on stress–strain curves and crack patterns in both loading directions match with experimental results very well.

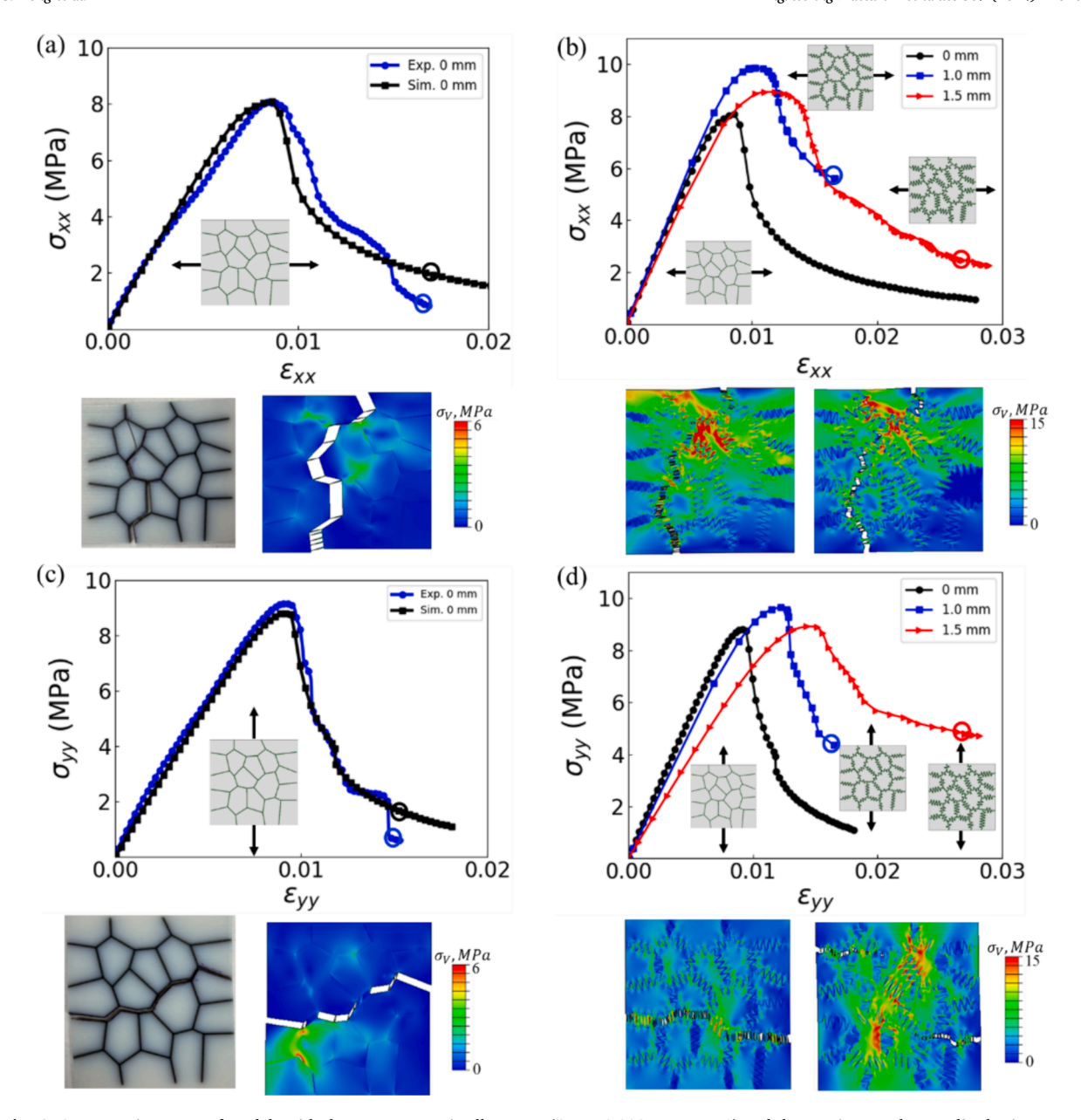


Fig. 4. Stress strain curves of models with the same Voronoi cell pattern ( $C_{std} = 0.002$  mm, R = 1) and the varying regular amplitudes in sutures. Experimental and simulation results for models with flat sutures (A = 0) under (a) X and (c) Y tension loadings, respectively. (b, d) Simulation results for models with different regular amplitudes in sutures of 0, 1.0, 1.5 mm under X and Y tension loadings, respectively. The fractured samples from both experimental and FE simulations are below the stress strain curves. The strains corresponding to the captured snapshots of fractured samples in both experiments and FE results are illustrated by circles. In the subsequent figures, unless otherwise specified, these snapshots of fractured samples are captured near the final strains.

To further evaluate the influences of suture amplitude on the overall mechanical responses of the designs, FE simulations were performed on designs with three different suture waviness by varying the amplitude A=0, 1.0, and 1.5 mm by using the same set of material parameters ( $C_{std}=0.002$  mm, R=1,  $A_{std}=0$ ). The FE results under uni-axial tension along X and Y directions are shown in Fig. 4b and 4d, respectively. It is demonstrated that in both X and Y directions, models featuring wavy suture layers exhibit notably higher peak stress and fracture toughness compared to that with flat suture layers. Furthermore, the higher amplitude of the suture layer allows for a more graceful post-failure process, with slower decrease in stress after the peak stress. For designs with higher suture amplitude, the effective stiffness slightly decreases, this is mainly because of the increase in the total volume fraction of the soft phase due to the increase in suture amplitude.

# 3.2. The effects of tile length aspect ratio R (Type II designs)

To explore the influence of tile length aspect ratio *R* on the overall mechanical responses of the designs, both FE simulations and experiments on 3D printed specimens of Type II designs were carried out. The FE and experimental results are shown in Fig. 5.

Fig. 5 shows the deformation responses of models featuring various aspect ratios under X and Y tensile loadings. The results indicate a notable influence of tile length aspect ratio R on peak stress, stiffness, and toughness. Specifically, under X tension loading in Fig. 5a, models with higher R exhibit larger failure strains but lower stiffness. While under the Y loading direction in Fig. 5b, increasing R enhances specimens' toughness, strength and slightly increases stiffness as well.

To further examine the mechanical properties of the model with R=3, for comparison, FE model of R=3 featuring flat sutures are set up. The stress–strain responses are shown in Fig. 6. The FE prediction on the overall stiffness ratio  $E_x/E_y$  for the flat suture model was calculated to be 0.56, while for the model with wavy sutures, it is 0.8. Thus, the models with wavy sutures exhibited less anisotropy than those with flat sutures.

To investigate the fracture process, we took the specimen with R=3 under X and Y tension loading as a representation. In Fig. 5c-d, the strain contours from DIC reveal that stress concentrations occurred in the short ridges and boundary regions in the designs. The damage parameter SDEG (overall stiffness degradation) serves as an indicator of the level of damage sustained by each element it traverses. A value of zero indicates that the element is undamaged, while a maximum value of 1 signifies fully degradation, leading to the deletion of the element as crack propagation initiates. Therefore, the SDEG damage parameter was employed to monitor the evolution of the fracture process zone. In Fig. 5c-d, the SDEG contours illustrate that damage initiates from the boundary regions in soft suture layer due to stress concentrations. Subsequently, fracture propagates mainly along the soft layer until complete separation occurs.

# 3.3. The effects of tile size irregularity C<sub>std</sub> (Type III designs)

In order to evaluate the irregularity of tile size, represented by the tile size standard deviation  $C_{std}$ , on the overall mechanical response of the designs. Both FE simulations and mechanical experiments are performed on 3D printed Type III designs. The FE and experimental results in X and Y directions are compared in Fig. 7 and Fig. 8, respectively.

Fig. 7a and 8a show that the stress–strain curves with  $C_{Std} = 0$ , 0.002 and 2 mm are close to each other in both X and Y directions.

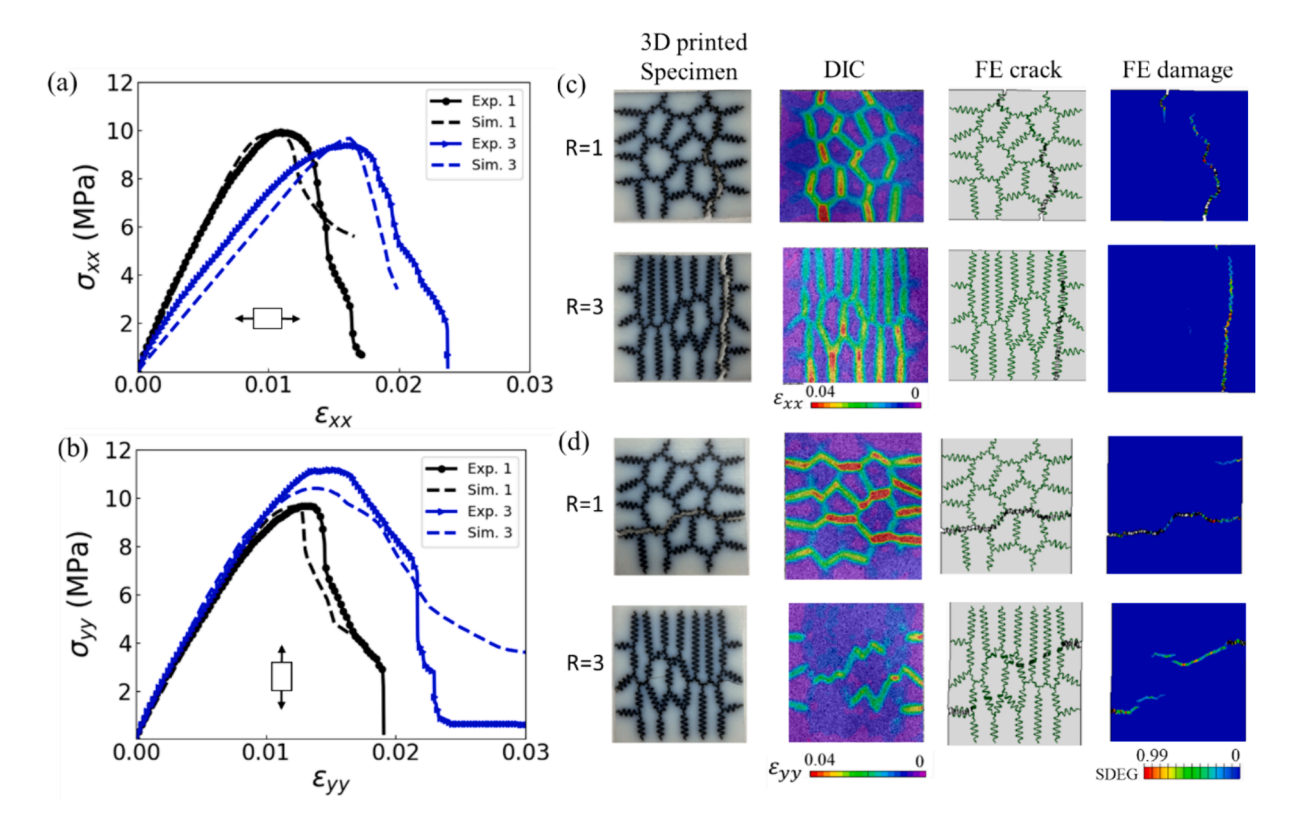


Fig. 5. Experimental and simulation stress strain curves for models with different aspect ratios of 1 and 3 under (a) X and (b) Y tension loadings, respectively. (c, d) Fracture evolution of models with R = 1 and R = 3 under X and Y tensile loading respectively. The first column is fractured 3D printed specimens. The second column is strain contours from DIC at the overall 0.2 % offsets strains. The third column displays fractured FE models, and the fourth column shows the FE damage of SDEG (overall scalar stiffness degradation).

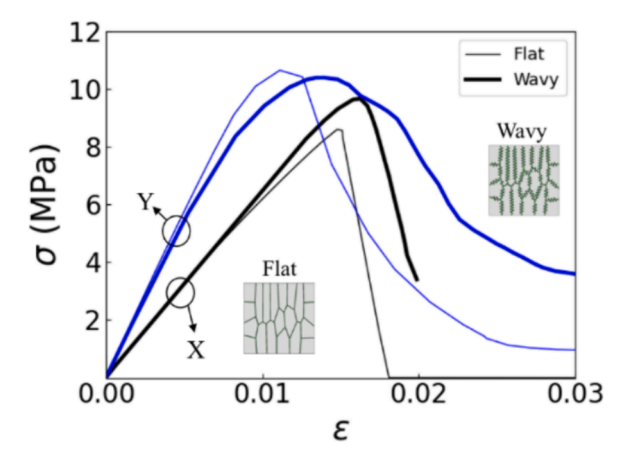
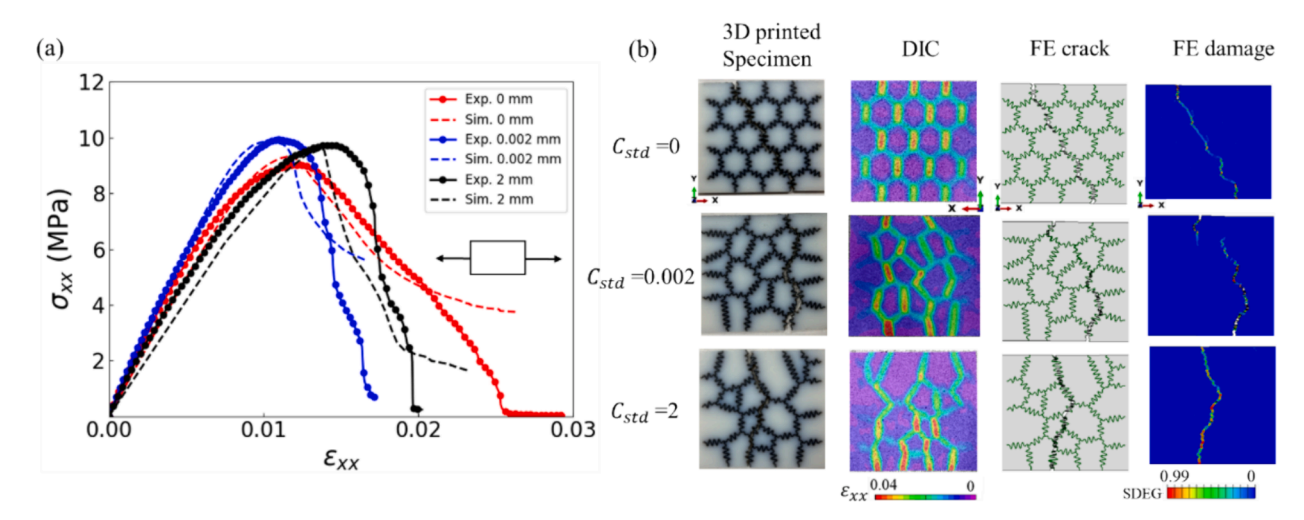


Fig. 6. The stress strain curves of models with R = 3 feature flat and wavy sutures under X and Y tensile loading respectively.



**Fig. 7.** (a) Stress strain responses from experiments and simulations of the models with  $C_{std} = 0$ , 0.002 and 2 mm, A = 1.0 mm and R = 1 under the X tension loading. (b) The first column is the fractured 3D printed specimens. The second column is the strain contours from DIC at the overall 0.2 % offsets strain. The third column is the fractured FE models. The fourth column is the FE damage of SDEG.

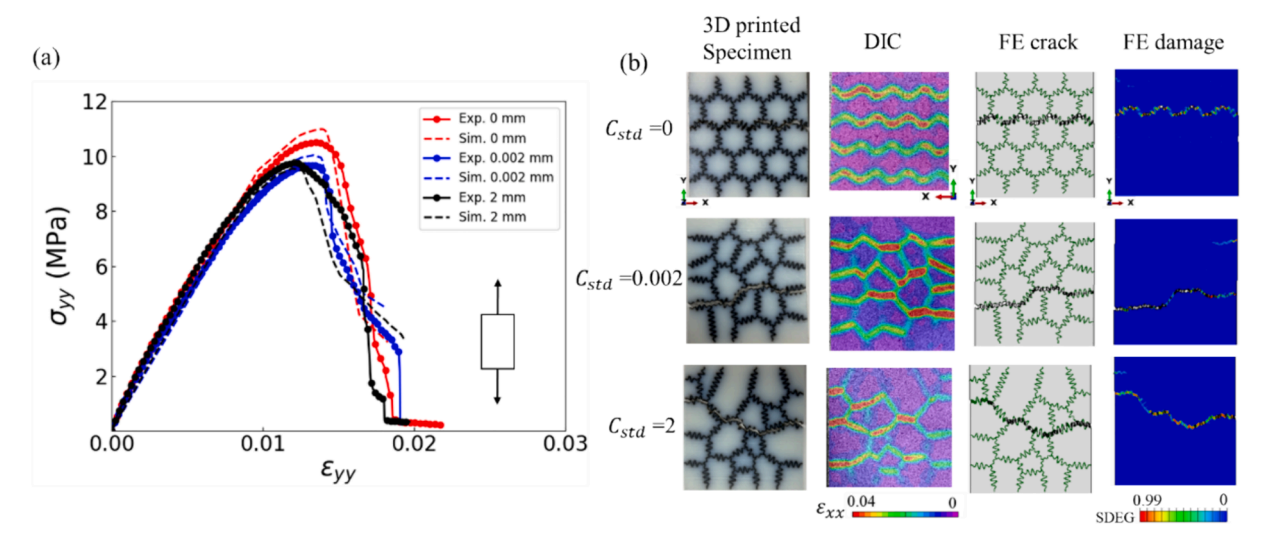
Specifically, all models have the comparable peak stress under X tensile loading and a very close stiffness and final failure strain under Y tensile loading.  $C_{Std}$  slightly influences the stiffness and ductility in X direction, and slightly influences the effective strength in Y direction.

Fig. 7b and Fig. 8b depict crack patterns and damage contours in experiments and FE simulation under uniaxial X and Y tensile loadings, respectively. Notably, the fracture regions observed in both experiments and simulations exhibit consistency. In both directions, the failure mode is dominated by suture layer failure. Roughly speaking, cracks propagate in suture layers perpendicular to the load directions.

# 3.4. The effects of suture irregularity (Type IV designs)

Since the suture layer thickness is a constant for all designs, suture irregularity is represented by the standard deviation  $A_{std}$  of suture amplitude. The investigation into the irregularity of the soft wavy sutures involves two scenarios with  $C_{std} = 0$  and 2 mm. We will evaluate the influences of  $A_{std}$  on designs with regular hexagonal tile pattern with  $C_{std} = 0$  and those with irregular tile patterns with  $C_{std} = 2$  mm. The FE models of two groups of designs are developed. The FE results for the group with regular tile pattern but irregular sutures are shown in Fig. 9. The FE results of Type IV designs (irregular tile pattern and irregular sutures) with  $A_{std} = 0$ , 0.1, 0.25 and 0.5 mm are conducted, and the results are compared in Fig. 10.

As shown in Fig. 9a, for models with  $C_{std} = 0$ , by introducing suture irregularity, the peak stress is reduced but the failure strain increased in X tension. Similarly, the suture irregularity helps increase fracture toughness without sacrificing a lot in peak stress under Y tensile loading (Fig. 9b). The Von mises stress contours at the final failure for each design are depicted in Fig. 9c-d, indicating that suture irregularity can more efficiently redistribute stress and alter crack propagation paths to avoid catastrophic failure.



**Fig. 8.** (a) Stress strain responses from experiments and simulations of the models with  $C_{std} = 0$ , 0.002 and 2 mm, A = 1.0 mm and R = 1 under the Y tension loading. (b) The first column is the fractured 3D printed specimens. The second column is the strain contours from DIC at the overall 0.2 % offsets strain. The third column is the fractured FE models. The fourth column is the FE damage of SDEG.

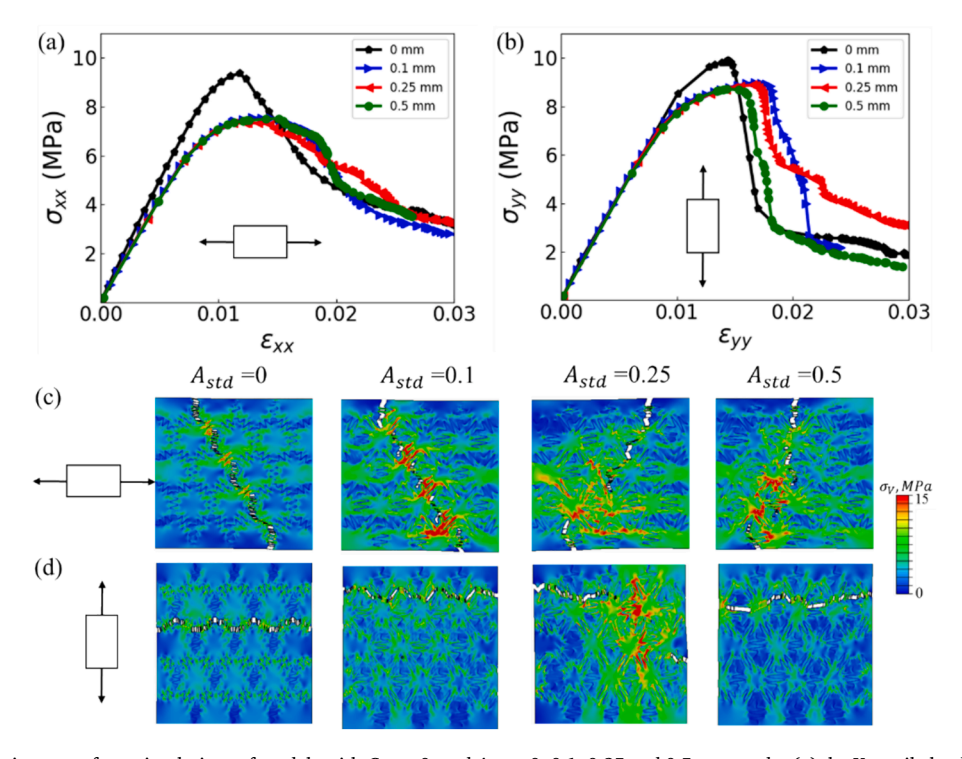
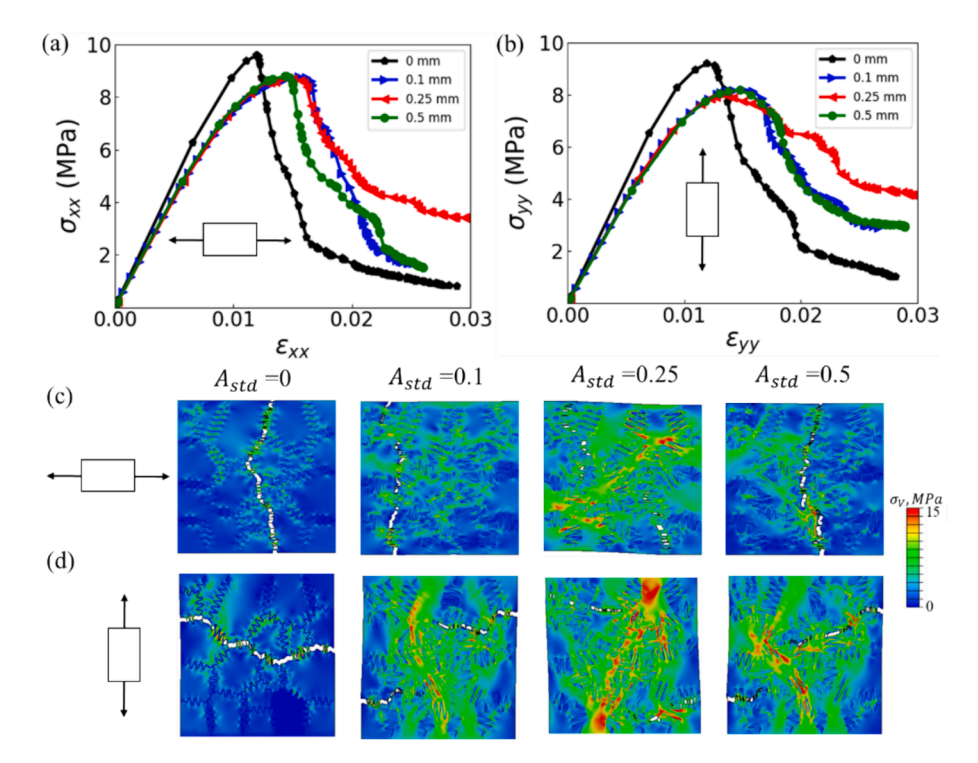


Fig. 9. Stress strain curves from simulations of models with  $C_{std} = 0$ , and  $A_{std} = 0$ , 0.1, 0.25 and 0.5 mm, under (a) the X tensile loading and (b) the Y tensile loading. (c, d) The Von mises stress contours of the fractured samples under the X and Y tensile loading, respectively.

To further understand the effects of suture irregularities for designs with irregular tile patterns, FE results on Type IV designs with  $C_{std}=2.0\,$  mm are shown in Fig. 10. Fig. 10a-b display the stress–strain curves for models subjected to X and Y tensile loading, respectively. The results show that suture irregularity can significantly increase the final failure strains under both X and Y tensile loadings with only a little decrease in effective strength. Fig. 10c-d show the diverse fracture paths associated with varying degrees of suture irregularities. In addition, in models with  $C_{std}=0$ , the cracks propagate faster under Y tension (in Fig. 9b) compared to X tension (Fig. 9a). However, for models incorporating Voronoi tile patterns (Fig. 10), fracture processes under X and Y tensile loadings exhibit comparable gracefulness.



**Fig. 10.** Stress strain curves from simulations of models with  $C_{std} = 2$  mm, and  $A_{std} = 0$ , 0.1, 0.25 and 0.5 mm, under (a) the X tensile loading and (b) the Y tensile loading. (c, d) The Von mises stress contours of the fractured samples under the X and Y tensile loading, respectively.

Since damage was consistently observed in the soft phase, Fig. 11 displays the FE contours of Von mises stress within the soft suture layers of models featuring  $C_{std}=0$  and 2 mm, along with suture irregularities at the overall strain of 0.2 % offsets. Under both X and Y tensile loadings (Fig. 11a-b), stress concentration is prominently observed and localized near the triple conjunctions, short ridges, or boundary regions particularly in cases with regular sutures and regular cell patterns. The stress in other locations is quite uniform, indicating potential catastrophic failure. Nevertheless, integrating suitable suture irregularity, as exemplified by cases with the soft suture  $A_{std}=0.25$  mm, results in stress redistribution and a reduction in concentrated stress locations. Thus, suture irregularities can influence final facture strains and toughness by promoting the relatively uniform stress distribution, thereby delaying the fracture process, especially under Y tensile loading for the regular hexagonal geometry.

# 3.5. Effective Poisson's ratio

Systematic FE simulations are performed to evaluate the influences of stiffness ratio  $E_h/E_i$  between the hard and soft phases, tile length aspect ratio R, tile size irregularity  $C_{std}$ , and suture irregularity  $A_{std}$ , on the effective Poisson's ratio  $v_{XY}$ , and  $v_{YX}$ . In all FE models, the Young's modulus and the Poisson's ratio of the soft interfacial wavy layer are consistent at  $E_i = 50$  MPa and  $v_i = 0.4$ , respectively. The Young's modulus of the hard phase varies from 100 to 400,000 MPa with a constant Poisson's ratio of 0.3 for all simulations. The FE results are shown in Fig. 12a-11f.

Fig. 12a and 12d show that in general, the effective Poisson's ratios are sensitive to the stiffness ratio. When stiffness ratio increases, the effective Poisson's ratio decreases. When the stiffness ratio goes beyond 1000–10,000, the effective Poisson's ratio can become negative. Also, the tile length aspect ratio leads to differences in  $\nu_{XY}$ , and  $\nu_{YX}$ . Notably, models with R=3 exhibit a significant difference in Poisson's ratio between the X and Y directions, and the stiffness ratio has a small effect on Poisson's ratio under the Y direction. However, the tile irregularity and suture irregularity only slightly influence the effective Poisson's ratio.

# 3.6. Overall stiffness and toughness

The influences of tile size irregularity and suture irregularity on the effective stiffness and toughness of the designs are summarized in Fig. 13. Fig. 13a-13c shows that in general, for designs with irregular tiles and regular sutures (Type III), or regular tiles and irregular sutures (Type IV), the normalized effective stiffness ( $E/E_h/f_h$ ) is not sensitive to either tile irregularity or suture irregularity. While the tile and suture irregularity will influence the overall toughness of the designs. The toughness is defined as the area underneath the overall stress–strain curves upto the point when the stress drops 60 % of the peak stress, as shown in Fig. 13d. Compared with tile irregularity, suture irregularity has larger influences on the toughness. As shown in Fig. 13e and Fig. 13f, when suture irregularity increases from 0 to 0.5 mm, the toughness increases first and then decreases, indicating an optimal level of irregularity for maximizing

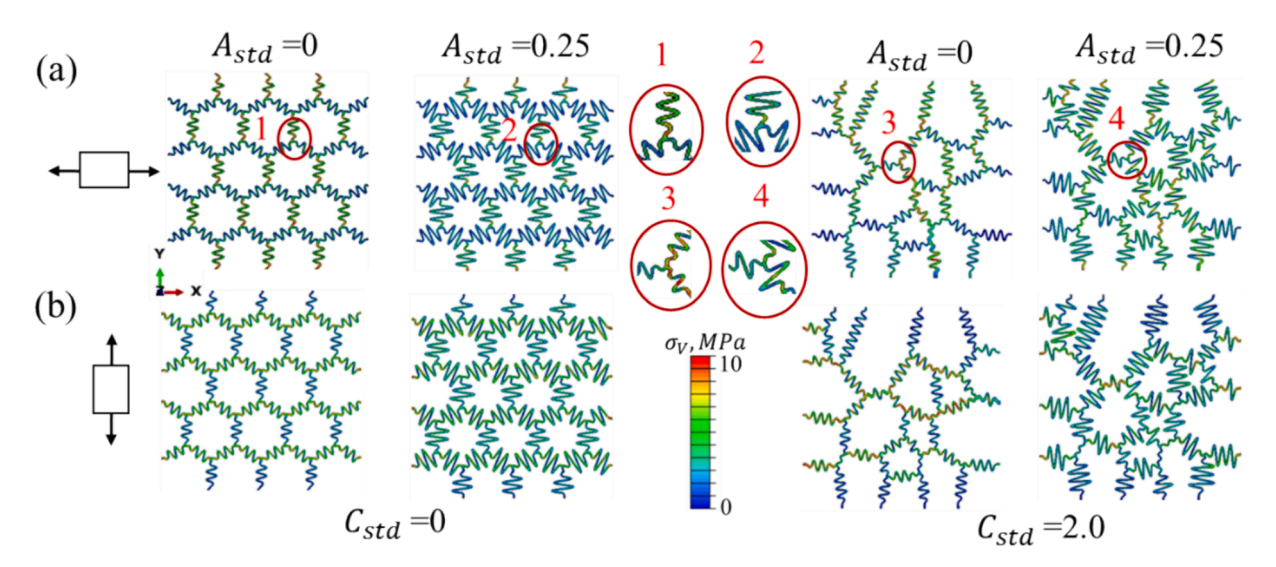


**Fig. 11.** The Von mises stress contours in the suture layers of models with  $C_{std} = 0$  and 2 mm at the overall strain of 0.2 % offset under (a) the X tensile loading and (b) the Y tensile loading.

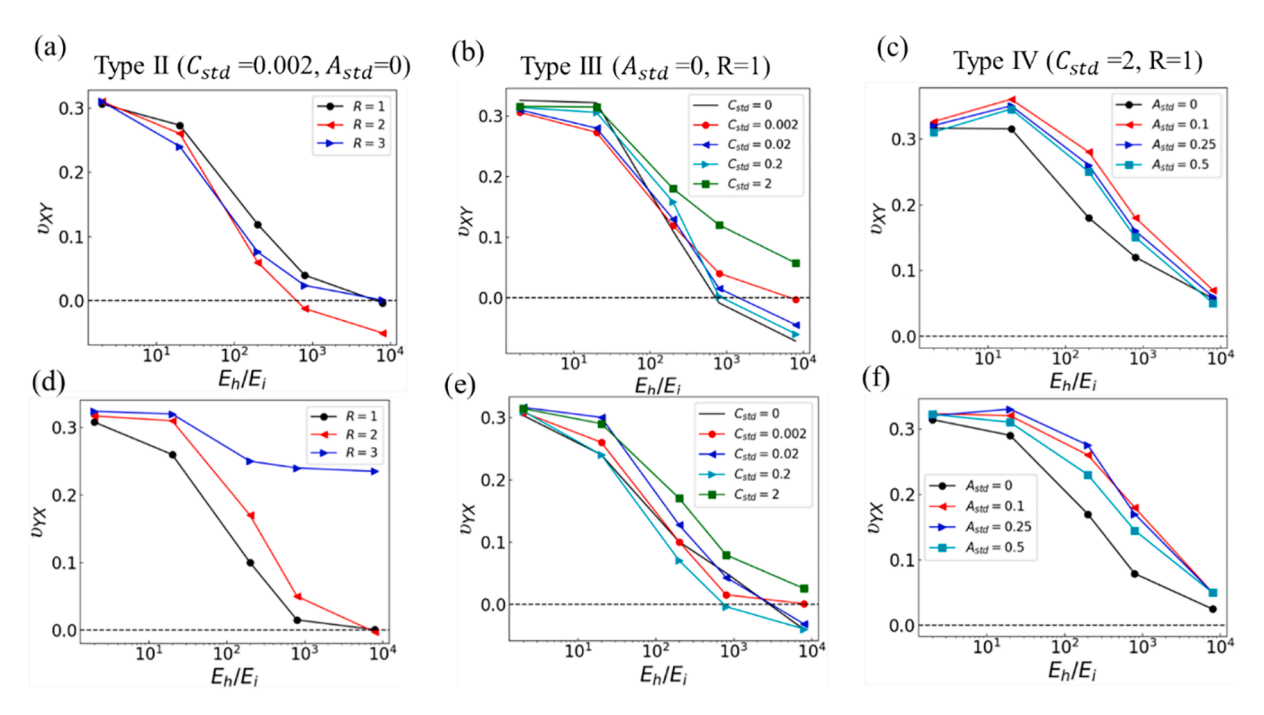


**Fig. 12.** (a-c) The influences of stiffness ratio  $E_h/E_i$ , tile length aspect ratio R, tile size irregularity, and suture irregularity on the effective Poisson's ratio  $\nu_{XY}$ , and (d-f)  $\nu_{YX}$ .

toughness. Roughly speaking, for the design space explored in this investigation, the optimal suture irregularity is between 0.2-0.3 mm.

## 4. Disscussion

Fracture behavior of the tiled composites can be broadly classified as ductile and brittle. Ductile berakage in the desings is characterized by extensive deformation occurring over a relatively prolonged period, often associated with yielding before eventual failure. In contrast, brittle breakage is preceded by minimal deformation, and typically occurs suddenly. Many catastrophic failures of structures can be attributed to some form of geometric discontinuity or stress concentration [45]. These discontinuities act as initiation sites for cracks, particularly under tensile loading. Emphasizing the attainment of progressive failure over sudden rupture is important

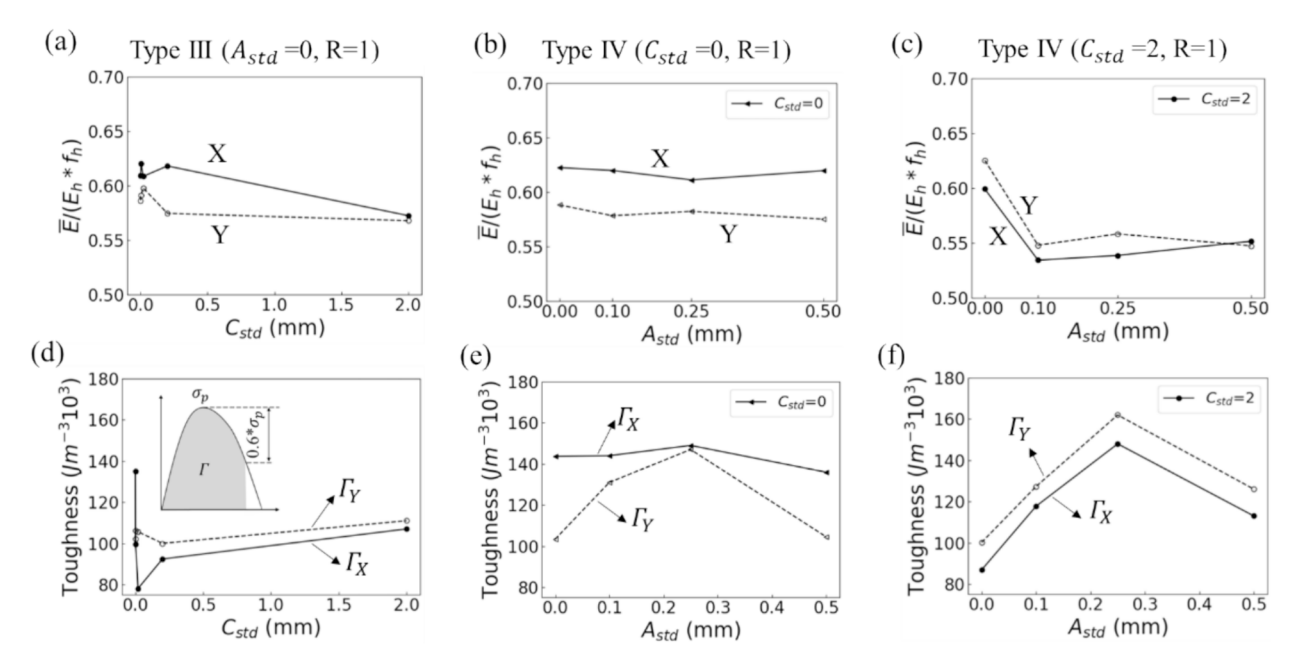


**Fig. 13.** (a-c) The influences of tile size irregularity and suture irregularity on the normalized effective stiffness  $(E/E_h/f_h)$ . (d-e) The influences of tile size irregularity and suture irregularity on overall toughness of the designs.

for enhancing toughness and energy absorption. It is equally crucial to redistribute the load at stress concentrations to minimize the risk of structural failure, which can be intensified by notch effects.

In experiments, variations in mechanical responses were observed, with localized deformation primarily occurring in the soft suture layers. Results suggest that brittle breakage usually exhibited single straight cracks, while ductile breakage featured deflected cracks, with fracture occurring in the interfacial region and often initiating from the boundaries. For example, specimens with  $C_{std} = 0$ , 0.002 and 2 mm (Fig. 8) under Y tensile loading exhibited brittle fracture behaviors, splitting into distinct parts under small strains (about 0.25 %). While most of the rest specimens displayed more ductile behavior with curvy cracks that did not result in complete separation. This process involves redistributing the load at stress concentrations to alter the pathway of structural failure.

The geometry of sutures plays a significant role in retarding cracks and delaying final failure. Irregular sutures, as seen in Figs. 9 and 10, demonstrated ductile behavior with crack propagation not leading to complete separation. The asymmetrical structures of Voronoi diagrams and irregular sutures led to stress redistribution, influencing fracture propagation. These irregularities can promote ductile behavior by causing multiple crack paths, which help to redistribute stress and delay complete failure. Short ridges in the suture geometry were particularly prone to stress concentrations, resulting in less effective energy dissipation and subsequent fracture initiation. Ductile behavior is preferable in applications requiring high fracture toughness. The ductile fracture process involves nucleation, growth, and coalescence of small cracks, which results in a gradual reduction in load carrying capacity. Specifically, the fracture usually nucleates from the interfacial boundaries and grows along the weak soft phase.

Generally, tessellations with wavy suture layers exhibit enhanced toughness due to crack deflection and energy dissipation via the wavy interfaces. Optimal suture irregularity ( $\sim$ 0.2-0.3 mm) further improves stress distribution and crack deflection. The overall strength of suture tessellations is not sensitive to suture irregularity but is influenced by the tile length aspect ratio; for example, the specimen with R = 3 under Y tension has slightly higher strength than that of those with smaller R values. Stiffness is slightly higher in specimens with smaller cell irregularity  $C_{std}$ .

# 5. Conclusions

Regular and irregular suture tesellations were designed and fabricated using a multi-matrial 3D printer via material jetting. Uniaxial tension measurements were conducted to characterize the effective mechanical properties of the designs. Systematic FE simulations were also performed for parametric study. The results show that for tessellations with wavy suture layer exhibit higher toughness compared to those with flat interfacial layers, without compromising stiffness or strength significantly. Also, suture irregularity has larger influences on the toughness than tile irregularity. In addition, an optimal level of suture irregularity exists for maximizing toughness. Roughly speaking, for the design space explored in this investigation, models with the suture irregularity of  $\sim$  0.2–0.3 mm exhibit the highest modulus of toughness (defined as the area underneath the stress–strain curve when the stress drops 60 % of the peak stress).

In contrast, for most of the designs the overall stiffness is not sensitive to either tile irregularity  $C_{std}$  or suture irregularity  $A_{std}$ . Notably, the tile length aspect ratio R significantly affects the overall stiffness with a clear difference between the stiffness in X and Y

directions. When R increases, a higher level of anisotropy in stiffness is expected. However, compared with designs with flat soft layers, the ones with wavy suture layers show less anisotropy.

Furthermore, the overall Poisson's ratios in both directions decrease with increasing stiffness ratio  $E_h/E_l$ . Some designs show negative Poisson's ratio when the stiffness ratio between hard and soft phases to beyond  $\sim 1000-10,000$ . For example, the design with R=2 exhibits a negative Poisson's ratio when the stiffness ratio exceeds approximately 8000. Either tile size irregularity or suture irregularity only have very limited influences on the effective Poisson's ratio.

In addition, for all designs, fractures initiate from the free boundary regions and propagate across ridges perpendicular to the loading direction. Within the design space explored in this investigation, fracture in the soft suture layers is the dominant failure mechanism. The crack path can be tuned by varying both tile irregularity and suture irregularity. The simulation and experimental results provide a general design guidline on high performing functionally graded two-phase tessellations.

# CRediT authorship contribution statement

**Shujing Dong:** Writing – original draft, Visualization, Validation, Methodology, Investigation, Data curation. **Richard J. Nash:** Writing – review & editing, Validation. **Yaning Li:** Writing – review & editing, Visualization, Supervision, Resources, Methodology, Funding acquisition, Conceptualization.

# Declaration of competing interest

The authors declare the following financial interests/personal relationships which may be considered as potential competing interests: Yaning Li reports financial support was provided by Yaning Li, Associate Professor, Northeastern University. Yaning Li reports financial support was provided by National Science Foundation. If there are other authors, they declare that they have no known competing financial interests or personal relationships that could have appeared to influence the work reported in this paper.

# Data availability

data are provided in the manuscript and the appendix

# Acknowledgements

This work was supported by the start-up funding for Y. L., the SPARK funding from Northeastern University, and National Science Foundation (NSF) via grant CMMI-2140223.

# Appendix A

The model parameters of the hard phase mainly refer to ref. [38]. To determine the mechanical properties of the soft interfacial phase, tensile tests were conducted on specimens featuring a flat interfacial layer. The in-plane thickness of the soft flat interface was set at 0.3 mm, consistent with the design of 3D printed tiled composites. Fig. A1 illustrates the dimensions of the specimen. The uniaxial tension experiment was performed at a strain rate of 0.001/s. The load displacement curve is shown in Fig. A2.

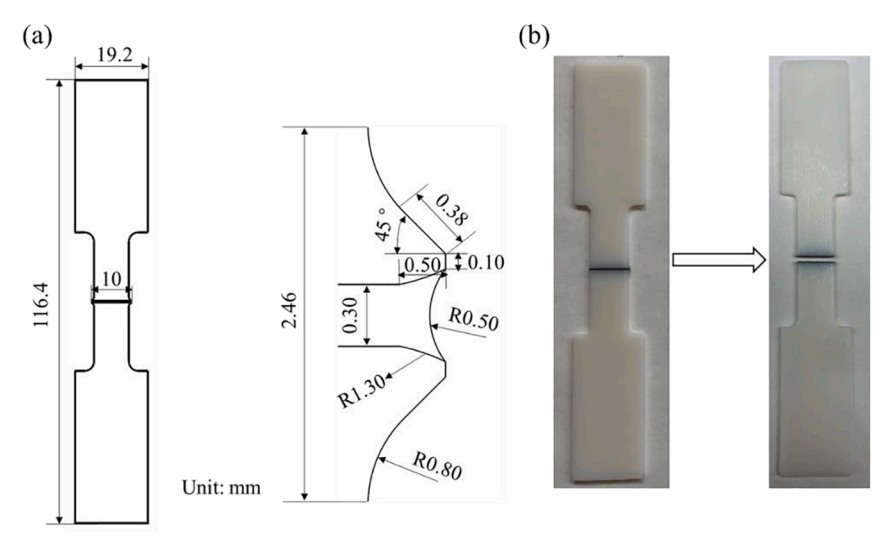


Fig. A1. (a) The dimensions of the specimens. (b) The 3D printed specimens before and after the tensile experiment.

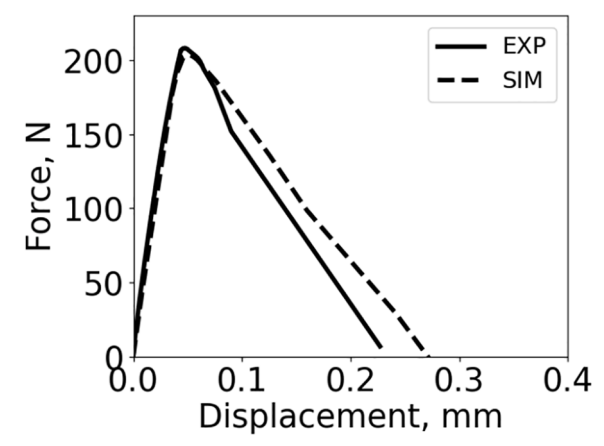


Fig. A2. The force and displacement curves of the specimen under uniaxial tensile loading.

In FE models, a power law plasticity model with an index n was employed to simulate the initial yielding and hardening of the hard phase. Additionally, a linear displacement damage evolution law, characterized by the final fracture strain  $\varepsilon_f$  and displacement, was utilized to capture the softening behaviors. For the soft interfacial phase, a bilinear plastic hardening model coupled with displacement based linear damage evolution was utilized to simulate the deformation behaviors. Models' parameters for both hard and soft phases were determined through careful calibration against experimental data. The model parameters are listed in Table A1.

**Table A1**Model parameters in FE simulations.

Materials	E (MPa)	$\sigma_{\rm y}({ m MPa})$	ν	$arepsilon_f$	dis.mm	n
Hard phase	1850	15	0.3	0.0154	0.5	0.71
Soft phase	50	11	0.4	0.2	0.25	_

# References

- [1] Aurenhammer F. Voronoi diagrams—a survey of a fundamental geometric data structure. ACM Computing Surveys (CSUR) 1991;23:345-405.
- [2] Okabe A, Boots B, Sugihara K, Chiu SN. Spatial tessellations: concepts and applications of Voronoi diagrams. 2009.
- [3] Aurenhammer F, Klein R. Voronoi Diagrams. Handbook of computational geometry. 2000;5:201-90.
- [4] Zhao H, Han Y, Pan C, Yang D, Wang H, Wang T, et al. Design and mechanical properties verification of gradient Voronoi scaffold for bone tissue engineering. Micromachines 2021;12:664.
- [5] Van Nuland T, Van Dommelen J, Geers M. An anisotropic Voronoi algorithm for generating polycrystalline microstructures with preferred growth directions. Comput Mater Sci 2021;186:109947.
- [6] Coster M, Chermant J-L. On a way to material models for ceramics. J Eur Ceram Soc 2002;22:1191–203.
- [7] Sung BJ, Yethiraj A. Structure of void space in polymer solutions. Phys Rev E 2010;81:031801.
- [8] Burtseva L, Werner F, Valdes B, Pestryakov A, Romero R, Petranovskii V. Tessellation methods for modeling the material structure. Appl Mech Mater 2015;756: 426–35.
- [9] Dong S, Zhou C. Plastic Deformation in Aluminum Columnar Nanograins. JOM 2023;1–9.
- [10] Diehl M. Review and outlook: mechanical, thermodynamic, and kinetic continuum modeling of metallic materials at the grain scale. MRS Commun 2017;7:
- [11] Fullwood DT, Niezgoda SR, Adams BL, Kalidindi SR. Microstructure sensitive design for performance optimization. Prog Mater Sci 2010;55:477–562.
- [12] Kumar K, Van Swygenhoven H, Suresh S. Mechanical behavior of nanocrystalline metals and alloys. Acta Mater 2003;51:5743-74.
- [13] Wang YM, Voisin T, McKeown JT, Ye J, Calta NP, Li Z, et al. Additively manufactured hierarchical stainless steels with high strength and ductility. Nat Mater 2018;17:63–71.
- [14] Wang S, Ding Y, Yu F, Zheng Z, Wang Y. Crushing behavior and deformation mechanism of additively manufactured Voronoi-based random open-cell polymer foams. Mater Today Commun 2020;25:101406.
- [15] Huang J, Jiang T, Liu C, Liu Y, Zheng G, Wang H, et al. Transition from horizontal expansion to vertical growth in the oyster prismatic layer. Biochem Biophys Res Commun 2021;563:47–53.
- [16] Gibson LJ. Biomechanics of cellular solids. J Biomech 2005;38:377–99.
- [17] Uraki Y, Tamai Y, Hirai T, Koda K, Yabu H, Shimomura M. Fabrication of honeycomb-patterned cellulose material that mimics wood cell wall formation processes. Mater Sci Engng C 2011;31:1201–8.
- [18] Nazzi F. The hexagonal shape of the honeycomb cells depends on the construction behavior of bees. Sci Rep 2016;6:28341.
- [19] Gutiérrez A, Gordon R, Dávila LP. Deformation modes and structural response of diatom frustules. J Mater Sci Eng Adv Technol 2017;15:105–34.
- [20] Danin A, Raus T. A key to 19 microspecies of the Portulaca oleracea aggregate: Moscow MV. Lomonosov State Univ.; 2012.
- [21] Lu H, Zhang J, Wu N, Liu K-b, Xu D, Li Q. Phytoliths analysis for the discrimination of foxtail millet (Setaria italica) and common millet (Panicum miliaceum). PLoS One 2009;4:e4448.
- [22] Krauss S, Monsonego-Ornan E, Zelzer E, Fratzl P, Shahar R. Mechanical function of a complex three-dimensional suture joining the bony elements in the shell of the red-eared slider turtle. Adv Mater 2009;21:407–12.
- [23] Yang W, Naleway SE, Porter MM, Meyers MA, McKittrick J. The armored carapace of the boxfish. Acta Biomater 2015;23:1-10.
- [24] Nash RJ, Li Y. Experimental and numerical analysis of 3D printed suture joints under shearing load. Engng Fract Mech 2021;253:107912.
- [25] Gao C, Li Y. Mechanical model of bio-inspired composites with sutural tessellation. J Mech Phys Solids 2019;122:190-204.

- [26] Liu L, Li Y, Failure mechanism transition of 3D-printed biomimetic sutures. Engng Fract Mech 2018;199:372-9.
- [27] Liu L, Li Y. Predicting the mixed-mode I/II spatial damage propagation along 3D-printed soft interfacial layer via a hyperelastic softening model. J Mech Phys Solids 2018:116:17–32.
- [28] Gao C, Li Y, Tuning the wrinkling patterns of an interfacial/coating layer via a regulation interphase. Int J Solids Struct 2017;104:92–102.
- [29] Liu L, Li Y. A visco-hyperelastic softening model for predicting the strain rate effects of 3D-printed soft wavy interfacial layer. Mech Mater 2019;137:103128.
- [30] Khoshhesab MM, Li Y. Mechanical behavior of 3D printed biomimetic Koch fractal contact and interlocking. Extreme Mech Lett 2018;24:58-65.
- [31] Cheon K-H, Gao C, Kang M-H, Jung H-D, Jang T-S, Kim H-E, et al. A crack-free anti-corrosive coating strategy for magnesium implants under deformation. Corros Sci 2018;132:116–24.
- [32] Pan HM, Chen S, Jang T-S, Han WT, Li Y, Song J. Plant seed-inspired cell protection, dormancy, and growth for large-scale biofabrication. Biofabrication 2019; 11:025008.
- [33] Hasseldine BP, Gao C, Li Y. Prediction of the anisotropic damage evolution of dry common millet (Panicum miliaceum) seed under quasi-static blunt indentation. Engng Fract Mech 2019;214:112–22.
- [34] Monsef Khoshhesab M, Li Y. The Strength of Dissimilar Fractal Joints. ASME International Mechanical Engineering Congress and Exposition. Am Soc Mech Engng 2016. p. V009T12A47.
- [35] Yang Y, Song X, Li X, Chen Z, Zhou C, Zhou Q, et al. Recent progress in biomimetic additive manufacturing technology: from materials to functional structures. Adv Mater 2018;30:1706539.
- [36] Quey R, Kasemer M. The neper/fepx project: free/open-source polycrystal generation, deformation simulation, and post-processing. In: IOP Conference Series: Materials Science and Engineering. IOP Publishing; 2022. p. 012021.
- [37] Sutton MA, Orteu JJ, Schreier H. Image correlation for shape, motion and deformation measurements: basic concepts, theory and applications. Springer Science & Business Media: 2009.
- [38] Quey R, Renversade L. Optimal polyhedral description of 3D polycrystals: Method and application to statistical and synchrotron X-ray diffraction data. Comput Methods Appl Mech Engng 2018;330:308–33.
- [39] Gao C, Hasseldine BP, Li L, Weaver JC, Li Y. Amplifying strength, toughness, and auxeticity via wavy sutural tessellation in plant seedcoats. Adv Mater 2018;30: 1800579
- [40] Liu L, Jiang Y, Boyce M, Ortiz C, Baur J, Song J, et al. The effects of morphological irregularity on the mechanical behavior of interdigitated biological sutures under tension. J Biomech 2017;58:71–8.
- [41] Gdoutos EE. Fracture mechanics: an introduction. Springer Nature; 2020.
- [42] Davis JR. Tensile testing. ASM international; 2004.
- [43] Fanella DA, Naaman AE. Stress-strain properties of fiber reinforced mortar in compression. Journal Proceedings1985. p. 475-83.
- [44] Nataraja M, Dhang N, Gupta A. Stress-strain curves for steel-fiber reinforced concrete under compression. Cem Concr Compos 1999;21:383–90.
- [45] Mohammadi S. Extended finite element method: for fracture analysis of structures. John Wiley & Sons; 2008.